


Majorana zero modes in a magnetic and superconducting hybrid vortex

Vedangi Pathak ¹, Sayak Dasgupta ^{1,2} and Marcel Franz¹

¹*Department of Physics and Astronomy & Stewart Blusson Quantum Matter Institute, University of British Columbia, Vancouver, British Columbia, Canada V6T 1Z4*

²*Institute for Solid State Physics, University of Tokyo, Kashiwa 277-8581, Japan*

 (Received 10 July 2022; revised 13 December 2022; accepted 13 December 2022; published 26 December 2022)

We propose and investigate a new platform for the realization of Majorana zero modes in a thin-film heterostructure composed of an easy-plane ferromagnet and a superconductor with spin-orbit coupling. The system can support an energetically favorable bound state comprising a magnetic vortex and a superconducting vortex. We show that a hybrid vortex thus created can host a robust zero-energy Majorana bound state at its core over a wide range of parameters, with its partner zero mode located at the boundary of a disk-shaped topological region. We identify a novel mechanism underlying the formation of the topological phase that, remarkably, relies on the orbital effect of the magnetization field and not on the usual Zeeman effect. The in-plane components of magnetization couple to electrons as a gauge potential with nonzero curl, thus creating an emergent magnetic field responsible for the gapped topologically nontrivial region surrounding the vortex core. Our construction allows the mobility of magnetic vortices to be imposed on the Majorana zero mode at the core of the superconducting vortex. In addition, the system shows a rich interplay between magnetism and superconductivity which might aid in developing future devices and technologies.

DOI: [10.1103/PhysRevB.106.224518](https://doi.org/10.1103/PhysRevB.106.224518)

I. INTRODUCTION

One of the primary thrusts in current condensed matter physics is the search for new platforms capable of supporting exotic quasiparticles of which the Majorana particle is of special significance. These emergent Majorana excitations are topologically protected against local perturbations and exhibit non-Abelian exchange statistics [1–3], making them ideal to store and manipulate quantum information via topological qubits [4].

Initial theoretical proposals [5] showed that edge states of a spinless p -wave superconductor in one dimension and correspondingly vortices in a spinless $p_x + ip_y$ phase in two dimensions will host Majorana zero modes. However, these systems do not occur naturally. Consequently, a large research effort was dedicated to realizing the same topological properties in more conventional systems leading to proposals involving the surface states of a topological insulator [6], semiconductor-superconductor heterostructures [7–9], chains of magnetic adatoms [10] and many more.

One possible and realistic implementation of topological p -wave superconductivity is in the form of superconducting heterostructures. Such heterostructures require the presence of a large superconducting gap, strong spin-orbit coupling (SOC), and a time-reversal breaking field to obtain an effective topological superconductor [7,9]. While a simple construction in principle, it was soon realized that it can be difficult to obtain semiconductor wires with large-enough SOC. This prompted alternate proposals where the need for an SOC was circumvented by exchange coupling the spins in the superconductor to noncollinear magnetic islands. In

particular, Choy *et al.* [10] showed that in the presence of a chain of magnetic adatoms, where the spins of the adatoms were not aligned, the s -wave order parameter converts to an effective spin polarized p -wave superconductor with Majorana modes at the end. This proposal was followed by a series of works where a similar s -wave-to- p -wave conversion was shown for a wire with a helical magnetic order, proximitized to an s -wave superconductor [11–13]. In these constructions the helical magnetic state is self-stabilized through an effective RKKY-type interaction mediated by the superconductor. An analogous construction was used by Nakosai *et al.* [14] to obtain a chiral p -wave superconductor in two dimensions by proximitizing an s -wave superconducting slab to a magnetic slab with a non-co-planar skyrmion-like arrangement of magnetic moments. In this chiral p -wave state, a vortex core was predicted to host a Majorana zero mode (MZM). Recent experiments have shown signatures of chiral topological phases in ferromagnetic islands [15,16].

Building on these efforts Yang *et al.* [17] constructed a heterostructure with a double winding skyrmion proximitized to an s -wave superconductor, which produced stable MZMs bound to the center of the skyrmion core. The isolation of the MZM from the other states in the vortex core was enhanced by increasing the winding. However, it is difficult to generate skyrmion textures with high winding numbers; if one tries to construct them by merging individual skyrmions with a single winding, then the skyrmions tend to energetically favor annihilation. What works is a heterostructure comprising a single winding skyrmion in the ferromagnetic layer bound to a superconducting vortex in the s -wave superconductor. This construction hosts an MZM at the vortex core and the

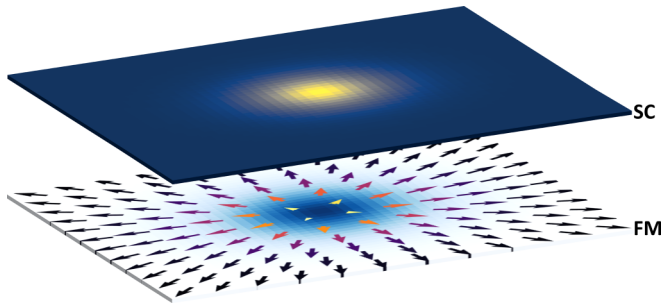


FIG. 1. System comprising a ferromagnet-superconductor heterostructure. The magnetic and superconducting vortex form an energetically favorable hybrid vortex which hosts Majorana modes.

skyrmion-vortex system is bound together through an exchange coupling [18].

The nature of the coupling between the magnetic texture and the proximitized superconductor was studied in Ref. [19], where the authors showed that the magnetic moments generate supercurrents which in turn generate the interaction between the superconducting vortex and the underlying magnetic texture. The current-current interaction reduces to an effective magnetoelectric potential with a strength proportional to the SOC and size of the magnetic moments. Hals *et al.* [20] used this term to produce an energetically stable bound state between a superconducting vortex and a magnetic skyrmion and further showed how this composite object can be manipulated by using a spin current to move the magnetic skyrmion in the magnet. The vortex being bound to the skyrmion core is dragged along [20]. These works proposed a setup where one could, at least theoretically, isolate an MZM and move it around freely.

Inspired by this, here we investigate conditions for the stability of a hybrid magnetic and superconducting vortex pair in a heterostructure composed of ferromagnetic and superconducting thin films shown schematically in Fig. 1. The magnetic vortex is a defect native to an easy plane ferromagnet, unlike the skyrmion, which exists as a soliton in the easy axis ferromagnet. Such systems are rare in the natural state but recent studies have shown that monolayer van der Waals materials such as NiPS₃ and CrCl₃ have strong easy plane character and nearly isotropic behavior within the easy plane [21–24].

Another route to magnetic vortices is through domain walls in two-dimensional uniaxial ferromagnets. For an easy axis in the xy plane we have domain walls which interpolate between two states via a magnetic vortex and half vortices [25]. These strips can be fairly wide (around 600 nm) which is an order of magnitude larger than the typical magnetic vortex radius (~ 10 nm) [26]. Thus we can isolate the vortex core in the center of the magnetic strip which then interacts with the superconducting vortex. A similar domain wall hosting a vortexlike spin structure can form in the triangular chiral antiferromagnets Mn₃X ($X = \text{Sn/Ge}$). There the local easy axis anisotropy creates a D_{3h} symmetric environment, producing six magnetic domains which meet at a vortex [27,28]. At the vortex core the magnetic normal mode structure ensures a spin canting out of the kagome plane which provides the necessary time-reversal breaking field to the superconducting

vortex [29]. The domain wall version of the magnetic vortex is easier to generate than an isolated magnetic skyrmion, typically generated by melting skyrmion crystals which exist in a very small temperature window of the phase diagram in a chiral magnet [30].

We want to couple the magnetic vortex to a superconducting vortex in an s -wave superconducting film. The superconducting gap of the order of 0.3–0.5 meV [16] is much smaller than the exchange interaction energies of the magnetic materials (particularly those where the vortex occurs at a domain wall) which are of the order of 10 meV [31]. So the magnetism is largely unaffected by the superconducting order parameter. In addition, the superconductor-ferromagnet heterostructure needs to have a Rashba interaction in order to form a bound state [19]. For an insulating ferromagnet this Rashba interaction can be sourced from the superconductor [32] or through an interfacial Dzyaloshinsky-Moriya interaction in the magnet. We use the former in our tight binding model. The coupling between the two systems can be modeled as an effective exchange interaction between the magnetic moments and the spins of the electrons in the superconductor [20]. This time-reversal symmetry breaking coupling is responsible for the topological property of the superconductor. Note that the magnetic field of the ferromagnet is confined to the magnetic layer and does not penetrate the superconductor, much like the electric field of a charged parallel plate capacitor.

We find that the magnetic vortex and the superconducting vortex cores comprising the hybrid vortex form an energetically favorable state and exhibit a strongly attractive behavior with an energy density that varies as a square of the core separation. The question then is whether such a system can host a Majorana bound state, without an external Zeeman field, localized at the hybrid vortex, which we find to be the case. Specifically one zero mode is located at the core of the hybrid vortex and its partner at the outer ring of the topologically nontrivial region centered at the core. We find that the topological phase inside the ring is enabled by an emergent orbital magnetic field effect and, interestingly, not by the Zeeman field as would be the case in conventional models [7,9]. Majorana bound states in such hybrid vortices are distinguished by their ease of manipulation via the magnetic textures and by scalability.

General conditions for stability of such a hybrid vortex are discussed in Sec. II B. Using a lattice model for this system (Sec. II A), we then investigate the presence of Majorana bound states in a stable hybrid magnetic and superconducting vortex pair (Sec. III).

II. HYBRID VORTEX

We consider a heterostructure made of an in-plane ferromagnet proximitized to an s -wave superconducting film. The ferromagnetic order parameter is represented by the magnetization field $\mathbf{m}(\mathbf{r})$ that is related to the spin field through the gyromagnetic ratio $\mathbf{m} = \gamma\mathbf{s}$. The magnetic soliton we want to couple to the superconductor is the vortex shown in Fig. 1. The corresponding magnetization configuration, detailed below, is a solution to the Heisenberg energy density functional in two spatial dimensions [33] and forms naturally without the need for Dzyaloshinsky-Moriya interactions. This is unlike

the skyrmion used in Rex *et al.* [18] and Hals *et al.* [20], which exists only in an easy axis Heisenberg ferromagnet with a substantial Dzyaloshinsky-Moriya interaction.

The magnetic vortex has spins mostly in the xy plane, except at the core of the vortex where the spins are forced to cant out of the plane by the exchange interaction. The magnetization field $\mathbf{m}(\mathbf{r})$ can be represented by a unit vector field with a magnetization of length M , $\mathbf{m}(\mathbf{r}) = M\hat{\mathbf{m}}(\mathbf{r})$. This length can be absorbed into the strength of the effective exchange between the magnetization and the spins of the superconductor. We denote the product of the two as a magnetic exchange coupling strength, m_0 . The orientation of the unit vectors is conveniently parametrized through two scalar fields, $\Theta(\mathbf{r})$ and $\Phi(\mathbf{r})$, representing the polar and azimuthal angles, respectively,

$$\hat{\mathbf{m}}(\mathbf{r}) = [\cos\Phi(\mathbf{r})\sin\Theta(\mathbf{r}), \sin\Phi(\mathbf{r})\sin\Theta(\mathbf{r}), \cos\Theta(\mathbf{r})]. \quad (1)$$

For the vortex centered at the origin the $\Theta(\mathbf{r})$ field obeys the boundary conditions $\Theta(\mathbf{r} \rightarrow \infty) = \pi/2$ and $\Theta(\mathbf{r} = 0) = 0$ or π . This is different from the magnetic skyrmion texture considered by Rex *et al.* [18] and Hals *et al.* [20], where the boundary conditions are $\Theta(\mathbf{r} \rightarrow \infty) = \pi$ (or 0) and $\Theta(\mathbf{r} = 0) = 0$ (or π). The $\Phi(\mathbf{r})$ field encodes the winding number defined as $2\pi n_m = \oint_C d\mathbf{r} \cdot \nabla\Phi$, where the integration contour is taken to enclose the vortex center. The winding number can be any integer, but we restrict ourselves to a singly quantized vortex or antivortex corresponding to $n_m = \pm 1$.

A. Microscopic model

We investigate the effect of coupling magnetic and superconducting vortices present in a two-dimensional heterostructure comprising a ferromagnet and an s -wave superconductor. Our microscopic model focuses on the superconductor, incorporating the effect of the underlying magnetic layer through an exchange coupling between the electron spins and the magnetic moment. The spin configuration of the magnet is considered to be frozen in this situation.

The Hamiltonian for an s -wave superconductor with spin-orbit coupling in a two-dimensional (2D) geometry can be written as $H = \int d^2\mathbf{r} \Psi^\dagger(\mathbf{r})\mathcal{H}(\mathbf{r})\Psi(\mathbf{r})$, where

$$\mathcal{H}(\mathbf{r}) = \left[-\frac{\nabla^2}{2m^*} - \mu + i\alpha(\sigma^y\partial_x - \sigma^x\partial_y) \right] \tau^z + m_0\hat{\mathbf{m}}(\mathbf{r}) \cdot \boldsymbol{\sigma} + \tau^x \text{Re}\Delta(\mathbf{r}) - \tau^y \text{Im}\Delta(\mathbf{r}), \quad (2)$$

with $\Psi^\dagger(\mathbf{r}) = [\psi_\uparrow^\dagger(\mathbf{r}), \psi_\downarrow^\dagger(\mathbf{r}), \psi_\downarrow(\mathbf{r}), -\psi_\uparrow(\mathbf{r})]$ the Nambu spinor. Here μ is the chemical potential, m^* denotes the effective electron mass, α is the Rashba spin orbit coupling, and $m_0 \propto M$ is an effective exchange coupling strength; σ^j and τ^j are Pauli matrices acting in spin and Nambu space, respectively.

A superconducting vortex with its center at $\mathbf{r}_s = (x_s, y_s)$ is modeled with open boundary conditions using the order parameter

$$\Delta(\mathbf{r}) = \Delta_0 \tanh\left(\frac{|\mathbf{r} - \mathbf{r}_s|}{2\xi_s}\right) e^{i\theta_s}, \quad (3)$$

where $|\mathbf{r} - \mathbf{r}_s|$ is the distance from the center of the vortex, ξ_s is the superconducting coherence length that controls the size

of the superconducting vortex, and θ_s is the phase winding around the vortex core. We define $\theta_s = n_s \tan^{-1}\left(\frac{y-y_s}{x-x_s}\right)$, where n_s is the vorticity. In the presence of the SC vortex, we can write $\nabla\theta_s = n_s \hat{\phi}_s / r_s$ where (ϕ_s, r_s) are polar coordinates in the frame where the superconducting vortex core lies at the origin.

To this we add the ferromagnet with a vortex centered at $\mathbf{r}_m = (x_m, y_m)$ with a magnetization profile parameterized as in Eq. (1). The helicity profile is chosen as $\Phi = n_m\phi + \varphi$ with ϕ the polar angle, n_m denoting its vorticity and φ being the helicity. In addition we take $\Theta(\mathbf{r}) = \frac{\pi}{2} \tanh(|\mathbf{r} - \mathbf{r}_m|/2\xi_m)$, with ξ_m controlling the size of the magnetic vortex core.

For numerical calculations it will be convenient to regularize the Hamiltonian Eq. (2) on the square lattice leading to the BdG lattice Hamiltonian of the form

$$H_{sc} = \sum_{\mathbf{r}, s, s'} \left\{ c_{\mathbf{r},s}^\dagger (4t - \mu) \delta_{ss'} c_{\mathbf{r},s'} + [c_{\mathbf{r},s}^\dagger (-t\delta_{ss'} - iu\sigma_{ss'}^y) c_{\mathbf{r}+\mathbf{x};s'} + \text{H.c.}] + [c_{\mathbf{r},s}^\dagger (-t\delta_{ss'} + iu\sigma_{ss'}^x) c_{\mathbf{r}+\mathbf{y};s'} + \text{H.c.}] \right\} + \sum_{\mathbf{r}} [\Delta_{\mathbf{r}} c_{\mathbf{r};\uparrow}^\dagger c_{\mathbf{r};\downarrow}^\dagger + \text{H.c.}]. \quad (4)$$

Here \mathbf{r} labels the coordinates of lattice sites, t is the nearest-neighbor hopping amplitude, $\Delta_{\mathbf{r}}$ is the superconducting pair field, and u is proportional to the spin-orbit coupling parameter, α . For the simulations in this paper, we take $u = \frac{\alpha}{2a}$, where the lattice constant, a , is 1. The exchange field of the ferromagnet is included as follows:

$$H_m = \sum_{\mathbf{r}, s, s'} c_{\mathbf{r},s}^\dagger [m(r)_j \sigma_{ss'}^j] c_{\mathbf{r},s'}, \quad (5)$$

where $\mathbf{m}(\mathbf{r})$ contains the spin texture of the ferromagnet. The Hamiltonian of the composite system is then

$$H = H_{sc} + H_m. \quad (6)$$

In the next part, we analytically study the interaction between a magnetic and superconducting vortex using an effective magnetoelectric free-energy density. We then compare our analytical results with full numerical simulations of the free-energy density using the composite Hamiltonian, Eq. (6). We find that in certain ranges of the SOC strength α and the magnetic exchange coupling strength m_0 we get a stable structure for a superconducting vortex bound to a magnetic vortex.

B. Magnetoelectric free energy

Our heterostructure explicitly breaks inversion symmetry which allows a Rashba SOC term in the superconductor. This SOC induces a corresponding magnetoelectric interaction between the supercurrent induced by the spin moments of the ferromagnet and the supercurrent density already present in the superconductor, say, from a vortex. Note that this current-current interaction can be obtained by considering an exchange-current interaction between the spin moments of each system and then integrating out the fermions through their propagator [19].

The coupling can be expanded in powers of the SOC strength α [19]. We now carry out the calculation of this energy density for a magnetic vortex interfaced with a superconducting vortex in order to study the stability of the bound state between the two defects. The linear coupling between the magnetization $\mathbf{m}(\mathbf{r}) = m_0 \hat{\mathbf{m}}(\mathbf{r})$, see Eq. (1), and the supercurrent $\mathbf{J}_s \propto \nabla \theta_s / 2 - \mathbf{A}$ is

$$F_{\text{ME}} = \kappa \int d\mathbf{r} (\hat{\mathbf{z}} \times \mathbf{m}) \cdot \left(\frac{\nabla \theta_s}{2} - \mathbf{A} \right), \quad (7)$$

where \mathbf{A} is the magnetic vector potential and $\kappa \propto \alpha$.

In the heterostructure we consider, we place a magnetic vortex at the origin. The profile of the magnetic vortex is given by $\mathbf{m}(\mathbf{r})$ with the boundary conditions on the Θ field chosen as $\Theta(r=0) = 0$ and $\Theta(r \rightarrow \infty) = \pi/2$. In addition, we have the Φ field vorticity, n_m , for a contour around the core. In the superconducting layer we assume an order parameter with a vortex core which can be displaced from the origin, $\theta_s = n_s \arctan[(y - y_s)/(x - x_s)]$. Here (x_s, y_s) is the location of the superconducting vortex core. This can be used to calculate the gradient of the phase in the planar polar coordinates,

$$\begin{aligned} \frac{\theta_s}{n_s} &= \arctan \left(\frac{r \sin \phi - r_s \sin \phi_s}{r \cos \phi - r_s \cos \phi_s} \right), \\ \nabla \left(\frac{\theta_s}{n_s} \right) &= \frac{(r - r_s \cos \tilde{\phi}) \hat{\phi} - 2r r_s \cos \tilde{\phi} \hat{\mathbf{r}}}{r^2 + r_s^2 - 2r r_s \cos \tilde{\phi}}, \end{aligned} \quad (8)$$

where $\tilde{\phi} = \phi - \phi_s$. In the limit where the penetration depth exceeds the core sizes $\lambda \gg \xi_m, \xi_s$, which will almost always be the case for thin SC films [34], we can ignore the screening currents $\mathbf{j} = -\mathbf{A}/4\pi\lambda^2$ induced by orbital [35] or dipolar magnetic fields [36]. In addition, since no magnetic field penetrates the superconductor we can take \mathbf{A} to be constant. In the following, we set $\mathbf{A} = 0$. This is similar to the assumption made by Hals *et al.* [20].

For the magnetic vortex we set the azimuthal field to $\Phi(r, \phi) = n_m \phi + \varphi$ and consider the situation where $n_m = 1$. The resulting free energy is given by

$$\begin{aligned} F_{\text{ME}} &= \kappa n_s m_0 f(r_{sm}) \cos \varphi, \\ f(r_{sm}) &= \pi \int_{r_{sm}}^{\infty} dr \sin \Theta(r), \end{aligned} \quad (9)$$

where r_{sm} (in our setup $r_{sm} = r_s$) is the separation between superconducting and magnetic vortex cores. Crucially, since we have a magnetic vortex where the Θ field varies between $[0, \pi/2]$, this integral is always positive definite. Thus the nature of the interaction, attractive or repulsive, between the two cores is controlled by the product $\kappa n_s m_0 \cos \varphi$.

Note that this term vanishes for $\varphi = \pi/2$ and is maximum for $\varphi = 0$. This can be anticipated from the supercurrent mediated interaction picture presented in Pershoguba *et al.* [19]. For $\varphi = 0$, the supercurrents induced by the magnetic vortex are *collinear* with the superconducting vortex supercurrents. This maximizes the interaction between the two. In the case of $\varphi = \pi/2$, the induced supercurrent density from the magnetic vortex is zero to first order in SOC, with some small second-order corrections, and hence we have negligible interaction. The transition between the two scenarios is shown in Fig. 5 and discussed in Sec. III in further detail. On evaluating the

integral in Eq. (9), for our chosen magnetization field, we find the interaction energy between the vortex pair is quadratic in the core separation r_{sm} , $F_{\text{ME}} \propto \xi_m (r_{sm}/\xi_m)^2$.

We can numerically calculate the free energy of the system using the tight-binding Hamiltonian Eq. (4). The free energy, F , of the BdG system is evaluated from the energy eigenvalues E_n using the standard formula,

$$F = -2k_B T \sum_n' \ln \left[2 \cosh \left(\frac{E_n}{2k_B T} \right) \right], \quad (10)$$

where the prime indicates summation over positive eigenvalues $E_n > 0$. In the limit of zero temperature, the above equation simplifies to $F_{T \rightarrow 0} = \sum_n' (-E_n)$. The formation of the hybrid vortex is energetically favorable if the free-energy minimum occurs when the superconducting and the magnetic vortex overlap, i.e., $r_{sm} \rightarrow 0$. The conditions for the formation of the hybrid vortex are summarized in Fig. 2. In these simulations, we fix the vorticity and the helicity of the magnetic vortex as $n_m = 1$ and $\varphi = 0$, respectively.

Taking F_0 as the free energy when $r_{sm} = 0$, we plot $\tilde{F} = F - F_0$ of the hybrid vortex as a function of distance between the magnetic and superconducting vortices in the region of stability for different parameter choices in Fig. 2. Matching our analytical prediction we see a quadratic dependence of the mutual interaction energy on the core separation, r_{sm} . Further, we observe that the minimum of \tilde{F} is stable at $r_{sm} = 0$ when the decay length of the magnetic vortex, ξ_m , is increased but the parabola becomes narrower, indicating that the coefficient of the quadratic interaction is dependent on ξ_m . Further, we observe that \tilde{F} remains nearly the same when the magnitude of the exchange coupling, m_0 , is increased with the minimum occurring at $r_{sm} = 0$ as expected.

We have also numerically verified the linear dependence of F_{ME} on α and m_0 . We observed that the variation with φ follows the cosine form near $\varphi = 0$ and $\varphi = \pi/2$ but deviates at other helicities due to the contribution of higher-order terms.

The second order in SOC term can be written down as

$$F_{\text{ME}}^{(2)} = \beta \int d\mathbf{r} (\nabla m_z \times \hat{\mathbf{z}}) \cdot \left(\frac{\nabla \theta_s}{2} - \mathbf{A} \right), \quad (11)$$

with $\beta \propto \alpha^2$. We can calculate this term in the same configuration with the magnetic vortex at the origin and the superconducting vortex at \mathbf{r}_s . We will take the limit $\mathbf{r}_{sm} (= \mathbf{r}_s) \rightarrow 0$ and look at the leading order in \mathbf{r}_{sm} correction. Setting $\mathbf{A} = 0$ as before the integral reduces to:

$$F_{\text{ME}}^{(2)} = \frac{\beta m_0}{2} \int d\mathbf{r} \sin \Theta(r) \left(\frac{\partial \Theta}{\partial r} \hat{\mathbf{r}} \times \hat{\mathbf{z}} + \frac{1}{r} \frac{\partial \Theta}{\partial \phi} \hat{\phi} \times \hat{\mathbf{z}} \right) \cdot \nabla \theta_s, \quad (12)$$

where $\nabla \theta_s$ is shown in Eq. (8). We can drop the second term $\partial \Theta / \partial \phi$ when the magnetic vortex is at the origin. The remaining integral can be evaluated after noting that $\hat{\mathbf{r}} \times \hat{\mathbf{z}} = -\hat{\phi}$, obtaining

$$2F_{\text{ME}}^{(2)} = \pi \beta m_0 n_s \left\{ \cos \left[\frac{\pi}{2} \tanh \left(\frac{r_{sm}}{2\xi_m} \right) \right] - 1 \right\}, \quad (13)$$

for $r_{sm} \leq \xi_m$ and $2F_{\text{ME}}^{(2)} = \pi \beta m_0 n_s$ for $r_{sm} > \xi_m$. To evaluate the exact forms we have used the magnetization profile shown in Eq. (1).

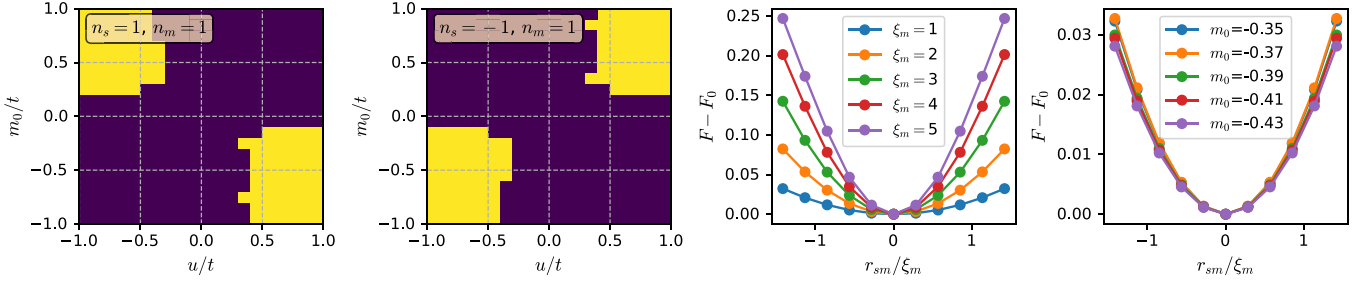


FIG. 2. Left two panels: Energetically favorable regions in parameter space for hybrid vortex formation. With the magnetic vortex texture ($\xi_m = 1$) fixed at the center of the system of size $L = 21$, the superconducting vortex core ($\xi_s = 1$) is moved along the diagonal starting at the position. The yellow shaded regions in all plots correspond to the points in the parameter space where the free-energy minima roughly correspond to the limit where the superconducting and the magnetic vortex are perfectly superimposed on each other (i.e., $r_{sm} = 0$) thereby forming a stable hybrid vortex. Regions of stability calculated for a magnetic vortex and superconducting vortex pair ($n_s = n_m = 1$) and for a magnetic vortex and a superconducting antivortex pair ($n_s = -1, n_m = 1$). Right two panels: Calculation of free energy of the hybrid vortex as a function of the distance between the magnetic and superconducting vortex. Here F_0 is the free energy when $r_{sm} = 0$. With the magnetic vortex texture fixed at the center of the system, the superconducting vortex core is moved along the diagonal. Free energy is plotted for different magnetic decay length parameters ξ_m at fixed $m_0 = -0.35$ and for different exchange coupling m_0 at fixed $\xi_m = 1$. The distance between the magnetic and the superconducting vortex is normalized with respect to ξ_m . Here $\Delta = 0.3$, $\mu = 0$, $t = 1$.

The second-order term is bound from above and can take a maximum value of $(\pi/2)\beta m_0 n_s$ unlike the first-order term. This in addition to the fact that it appears at a higher order in SOC ensures that the first-order term dominates except when $\varphi \rightarrow \pi/2$. Since $F_{\text{ME}}^{(2)}$ is independent of the helicity φ of the magnetic vortex it dominates when $\varphi \rightarrow \pi/2$ where F_{ME} vanishes [see (7)]. Even in this situation this term is not sufficiently large enough to produce a stable bound state between the two vortices according to our numeric simulations of the free energy.

C. Motion of the bound state

One of the key engineering features of binding superconducting vortices carrying an MZM to the magnetic vortex is that we can now propel the magnetic vortex in its own layer and hence propel the MZM. One has to take care that the vortices are still bound to each other during the process, and this can be ensured that the intercore distance, r_{sm} does not exceed the effective radius of the magnetic vortex, controlled by ξ_m . Within these bounds we use the effective interaction between the two cores

$$\mathcal{U}_{\text{int}} = \frac{k}{2} (\mathbf{r}_m - \mathbf{r}_s)^2, \quad (14)$$

where one can extract the value of the spring constant k from our tight binding model. As mentioned above it is dependent on the decay length of the magnetic vortex but is independent of the exchange coupling parameter.

For our case we analyze the effect of a spin current in the magnetic layer, following Hals *et al.* [20]. The equations of motion and the steady-state velocity are similar for us, with the skyrmion gyroscopic term replaced by that of the vortex. Notably, the magnetic vortex does not have an inertial mass unlike the magnetic skyrmion and obeys the Thiele equations [37,38]. Let us first look at the system in the absence of any damping:

$$\begin{aligned} \mathbf{G}_m \times [\dot{\mathbf{r}}_m - \mathbf{v}] &= -k(\mathbf{r}_m - \mathbf{r}_s) \\ m_s \ddot{\mathbf{r}}_s + \mathbf{G}_s \times \dot{\mathbf{r}}_s &= -k(\mathbf{r}_s - \mathbf{r}_m), \end{aligned} \quad (15)$$

where $\mathbf{G}_m = 2\pi S n_s p \hat{\mathbf{z}}$ is the gyroscopic tensor for the magnetic vortex, with S as the spin density and p as the polarization, $\text{sgn}(m_z)$, of the magnetic core. The superconducting cortex gyroscopic term, $\mathbf{G}_s = 2\pi \rho_s n_s \hat{\mathbf{z}}$, with ρ_s as the superfluid density. The spin current is an external spin polarized current adiabatically coupled to the ferromagnetic layer [39]. It enters as a correction to the time derivative in the equation of motion of the magnetic vortex and is represented by a velocity \mathbf{v} [40]. In the case of a standard magnetic insulator-like permalloy $|\mathbf{v}| = \hbar P j / (2eS)$, where j is the external current density.

In the steady-state limit, $\ddot{\mathbf{r}}_s = 0$, with $\dot{\mathbf{r}}_s = \dot{\mathbf{r}}_m = \dot{\mathbf{r}}$, i.e., the cores move together. We obtain

$$(\mathbf{G}_s + \mathbf{G}_m) \times \dot{\mathbf{r}} = \mathbf{G}_m \times \mathbf{v}, \quad (16)$$

leading to a steady-state velocity of $|\dot{\mathbf{r}}| = |\mathbf{v}| [G_m / (G_s + G_m)]$. In the presence of Gilbert damping and fieldlike damping from the spin current the steady-state velocity is modified. Going back to the original equations of motion, Eq. (15), in steady state, without the assumption $\dot{\mathbf{r}}_s = \dot{\mathbf{r}}_m$, we can see that a situation with $G_m = -G_s$ would result in a steadily growing core separation. This, however, requires fine-tuning the systems and is not generic. The strong attraction between the two cores also creates a situation where a drifting superconducting vortex can bind and carry a magnetic vortex, providing long-range dissipation-free spin transport. This schematic has been sought after in spintronics, and other proposals with magnetic vortices carrying spin currents have been proposed Kim *et al.* [41].

III. MAJORANA MODES

Majorana bound states (zero modes) are expected to be localized at the cores of vortices in two-dimensional superconductors which have a significant spin orbit coupling to mimic spinless fermions and are acted on by a Zeeman-like field to break the time reversal symmetry [7–9]. This Zeeman field is essential for accessing the topological region for a pure two-dimensional superconductor. However, for a hybrid vortex, the

proximitized spin texture breaks the time-reversal symmetry without an external Zeeman field and induces a manner of spin polarization. We show here that the system with the hybrid vortex hosts Majorana bound states. One of these states is localized at the vortex core while the other is at the edge of the disk-shaped topological region centered at the vortex. As we shall explain, the nontrivial topology in a system with a hybrid vortex originates from a novel *orbital* effect mediated by an emergent magnetic vector potential induced by the magnetic vortex.

In simple models with parabolic form of the kinetic energy it is possible to establish the existence of the vortex core modes by analytic calculations following the classic work of Caroli, de-Gennes, and Matricon (CdGM) [35] or by semiclassical approaches [42]. In our present case obtaining such analytical solutions for a hybrid vortex becomes difficult because of the more complicated form of the kinetic energy Eq. (2) combined with the presence of the spatially nonuniform magnetization field $\mathbf{m}(\mathbf{r})$. As explained below it is nevertheless still possible to unambiguously establish the presence of Majorana zero modes in the hybrid vortex by a combination of adiabatic continuity arguments and exact numerical diagonalization using the lattice version of the Hamiltonian Eq. (4).

To demonstrate the presence of MZM in our model we begin by considering what we call a “pure superconducting” vortex configuration; this consists of a conventional Abrikosov vortex coupled to the magnetic layer with a *uniform* magnetization along the $\hat{\mathbf{z}}$ direction. We observe that in this limit the Hamiltonian (2) coincides with the model studied by Cheng, Lutchyn, Galitski, and Das Sarma in Ref. [43]. A direct analytical solution in this limit is available and shows that a single unpaired MZM is present in the vortex core when

$$m_z^2 > \Delta_0^2 + \mu^2. \quad (17)$$

In the following we confirm this result numerically by observing a zero-bias peak in the local density of states (LDOS) defined as

$$\rho_{\mathbf{r}}(E) = \sum'_{\sigma,n} [|u_{r\sigma}^n|^2 \delta(E_n - E) + |v_{r\sigma}^n|^2 \delta(E_n + E)]. \quad (18)$$

Here the eigenvector at energy E_n of the BdG Hamiltonian assumes the form $\psi_{\mathbf{r},n} = (u_{\mathbf{r}\uparrow}, u_{\mathbf{r}\downarrow}, v_{\mathbf{r}\downarrow}^*, -v_{\mathbf{r}\uparrow}^*)_n^T$ (see Appendix A 1). Note that the spin polarized LDOS can be obtained using the same equation without the summation over the spin degrees of freedom, σ .

The second step in our argument consists of adiabatically deforming the uniform magnetization configuration into a magnetic vortex configuration which transforms the pure superconducting vortex into the hybrid vortex. Mathematically, this is achieved by smoothly evolving the spin texture defined in Eq. (1) between the two configurations. We start with $\xi_m \rightarrow \infty$, corresponding to a uniform magnetization, and then reduce ξ_m to a value smaller than the system size, which produces the hybrid vortex. If throughout this evolution the numerically observed zero mode remains present and separated by a gap from the rest of the spectrum, then we may conclude that it is adiabatically connected to the MZM in the pure SC vortex and therefore must be regarded as a Majorana mode. To further test this conclusion we perform additional

checks on the symmetry of the zero mode wave function which unambiguously distinguish it from the trivial CdGM state.

A. Pure superconducting and magnetic vortex

When only the superconducting vortex is present, a Zeeman field is required to stabilize the topological phase. This setup is equivalent to the system described by the BdG Hamiltonian in Eq. (2) in the limit where the magnetic vortex decay length is $\xi_m \rightarrow \infty$, which implies $\mathbf{m} = m_0 \hat{\mathbf{z}}$. The resulting model is identical to the Hamiltonian studied in Ref. [43], which is known to support a topological phase when Eq. (17) is satisfied. As a result, a Majorana zero mode is present in the vortex core and, in a finite system, its partner is localized at the outer edge of the sample.

The local density of states for this system, shown in Figs. 3(a) and 3(b), reveals a prominent zero bias peak localized at the vortex core, which we identify as MZM. The spin polarization in the LDOS is expected due to the time-reversal breaking Zeeman field provided by m_z in this case.

Now we consider a complementary configuration with a magnetic vortex and uniform superconducting order parameter. We will use this configuration to deduce the presence of an emergent orbital magnetic field \mathcal{B} that will play an important role in our understanding of the formation of the topological phase in our heterostructure. A numerical simulation of this situation reveals a high density of states near zero energy in the spectrum. This is evident in Fig. 3(c) where the distinct Majorana zero-bias peak in the LDOS is absent but a large number of low-lying excitations dominate the spectrum. Figure 3(d) indicates that these are concentrated along a ringlike structure surrounding the magnetic vortex. The presence of low-energy excitations suggests that the excitation gap vanishes at the ring, as would be the case if this were a boundary between a topological and a trivial phase. However, because $\xi_m = 1$ in this plot, the magnetization is entirely in plane long before one reaches the ring and the condition Eq. (17) cannot explain the apparent topological phase inside the ring. As we argue below, the topological phase inside the ring owes its existence to a novel orbital effect associated with the spatially varying magnetization field in the vicinity of the vortex center.

As explained in Refs. [7,9] the existence of the topological phase in the general class of models considered here depends on the nature of the excitation gap at the origin of the momentum space $\mathbf{p} = 0$. We thus examine the low-energy effective Hamiltonian obtained by expanding Eq. (2) to leading order in small momenta,

$$H_{\text{eff}} = \alpha(\boldsymbol{\sigma} \times \mathbf{p})_z \tau_z + \Delta_0 \tau_x + (\mathbf{m} \cdot \boldsymbol{\sigma}) \tau_0, \quad (19)$$

where $\mathbf{m} = (m_x, m_y, m_z)$. This can be rearranged into a more revealing form,

$$H_{\text{eff}} = \left(\begin{array}{cc} \alpha[\boldsymbol{\sigma} \times (\mathbf{p} - \mathcal{A})]_z & \Delta_0 \\ \Delta_0 & -\alpha[\boldsymbol{\sigma} \times (\mathbf{p} + \mathcal{A})]_z \end{array} \right) + m_z \sigma_z, \quad (20)$$

where we have identified the in-plane magnetization with an emergent gauge potential $\mathcal{A} = (\frac{m_y}{\alpha}, -\frac{m_x}{\alpha}, 0)$ minimally coupled to Dirac electrons. The electrons, therefore, can be

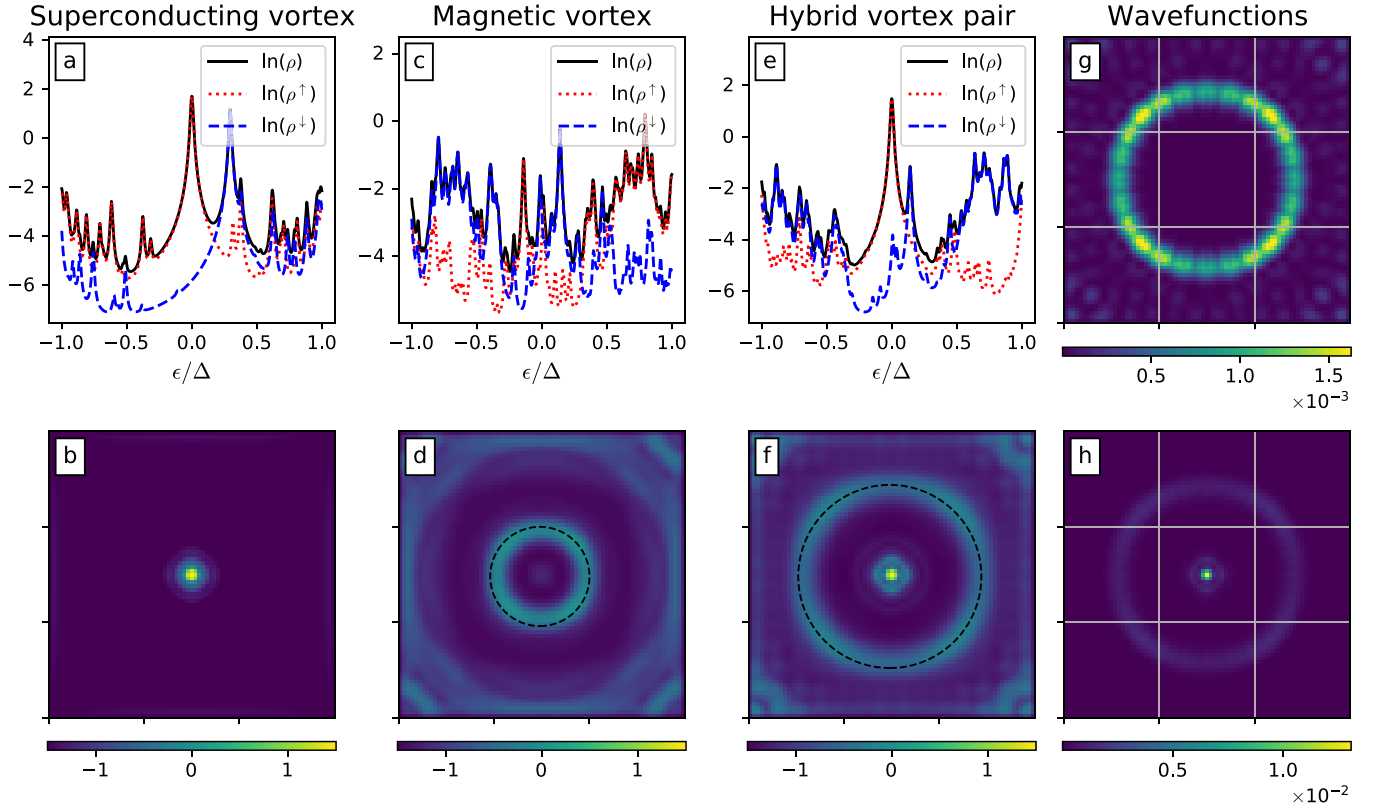


FIG. 3. [(a) and (b)] System with only superconducting vortex with external Zeeman field [equivalent to hybrid vortex with $\xi_m \rightarrow \infty$]. (a) The LDOS, $\rho(r_s, \epsilon)$, shows prominent zero-bias peak corresponding to Majorana zero modes. Spin-polarized LDOS reveals that the main contribution to the central Majorana zero-bias peak is from the spin-up LDOS. (b) The 2D plot shows LDOS ($\log[\rho(r, \epsilon = 0)]$) plotted at zero energy shows a Majorana mode localized at the vortex core. [(c) and (d)] System with only magnetic vortex (with $\xi_m = 1$) without any superconducting vortex. (c) LDOS at the vortex core shows that there is no isolated zero-bias peak. (d) The LDOS plotted at zero energy shows a ringlike structure (R_{mv}) surrounding the vortex core. The black dotted circle depicts the radius at which the local excitation gap vanishes [see Eq. (22)]. [(e)–(h)] System with hybrid vortex ($\xi_m = \xi_s = 1$). (e) The LDOS, $\rho(r_s, \epsilon)$, shows prominent zero-bias peak corresponding to Majorana zero modes. Spin-polarized LDOS reveals that the main contribution to the central Majorana zero-bias peak is from the spin-up LDOS, as expected when $n_s = n_m$. (f) The 2D plot shows LDOS ($\log[\rho(r, \epsilon = 0)]$) plotted at zero energy shows a Majorana mode localized at the vortex core. Additionally, there is a ring (radius R_{nv}) surrounding the core where the excitation gap vanishes. The radius, shown by the dotted black circle, is estimated where the local excitation gap in equation Eq. (B6) vanishes. [(g) and (h)] The decoupled wave-function probabilities, $|\phi_e|^2$ and $|\phi_c|^2$, corresponding to the two zero modes show that one Majorana mode is localized at the core while the other is present at the outer ring surrounding the vortex. Parameters: $L = 75$, $\Delta = 0.3$, $m_0 = -0.35$, $\varphi = 0$, $u = 0.6$, $\mu = 0$, $t = 1$.

thought of as moving in an emergent magnetic field $\mathcal{B} = \nabla \times \mathcal{A}$. This field can be calculated explicitly, away from the vortex core, using the magnetic texture $\hat{\mathbf{m}} = (\cos \Phi, \sin \Phi, 0)$ with $\Phi = \phi + \varphi$. Here the core is placed at the origin and φ is the helicity discussed in Sec. II B. This gives

$$\mathcal{B} = \frac{n_m m_0}{r} \cos \varphi \hat{\mathbf{z}}. \quad (21)$$

It is well known that application of a uniform magnetic field $\mathbf{B} = \hat{\mathbf{z}}B$ to Dirac electrons in 2D rearranges their spectrum into a set of discrete Landau levels, thus creating an excitation gap $\propto \sqrt{B}$. Here, according to Eq. (21), we are dealing with a nonuniform magnetic field that decays as $1/r$ away from the vortex center. Accordingly, in a semiclassical approximation we might expect the emergent field \mathcal{B} to produce an excitation gap $\propto 1/\sqrt{r}$ locally. Then, in analogy with Eq. (17), the ring observed in Fig. 3(d) can be interpreted as marking the edge of the topological region, where the magnetic gap dominates over the SC gap.

To find the radius of the ring, we estimate in Appendix B the size of the energy gap produced by the emergent magnetic field away from the vortex core. This local excitation gap, E_g , to lowest order in spin field gradients reads

$$E_g^2 = |\Delta_0^2 + m_0^2 - 2\sqrt{\Delta_0^2 m_0^2 + u^2 \mathcal{B}^2}|. \quad (22)$$

The excitation gap E_g vanishes at a radius R_{mv} marking the topological region. This coincides with the radius of the ring in the LDOS simulation shown in Fig. 3(d). In the subsequent discussion, it will be clear that these ringlike features are essential in the characterization of the topological regions for the hybrid vortex.

B. Hybrid vortex

Now we explore the characteristics of the low-lying modes present in the hybrid vortex. We consider the case where the magnetic and superconducting vortex have a similar core size ($\xi_m = \xi_s = 1$) and choose m_0 such that $m_0^2 > \Delta_0^2 + \mu^2$ at the

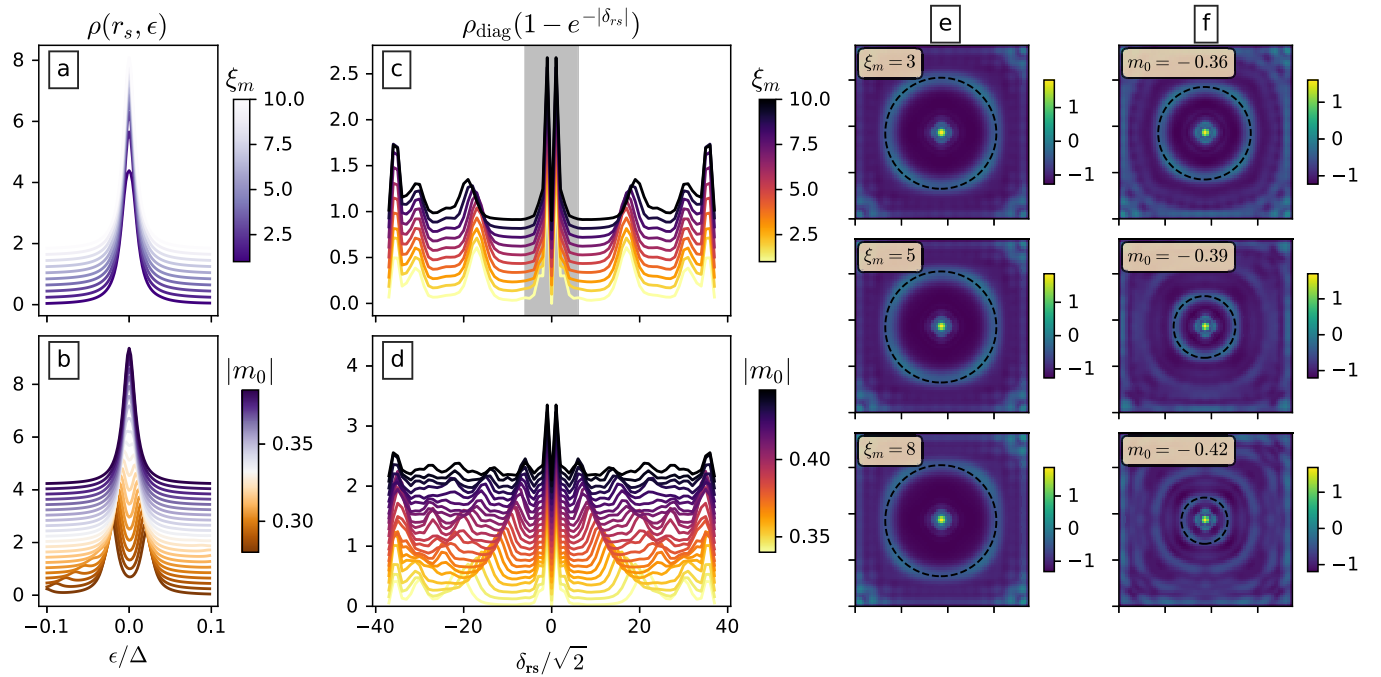


FIG. 4. Numerical simulations of a hybrid vortex on a 75×75 lattice. (a) The LDOS, $\rho(r_s, \epsilon)$, for varying magnetic vortex decay lengths ξ_m and fixed exchange coupling strength, $m_0 = -0.35$. (b) LDOS at the vortex core for varying exchange coupling, m_0 , at fixed magnetic vortex decay length, $\xi_m = 1$. LDOS exhibits a zero-bias peak for $|m_0| \gtrsim 0.33$. Parameters: $L = 75$, $\Delta = 0.3$, $\xi_s = 1$, $u = 0.6$, $\mu = 0$, and $t = 1$. (c) LDOS at different values of magnetic vortex decay length, ξ_m (with $m_0 = -0.35$). The plot shows a diagonal cross section of the LDOS at zero energy for different values of ξ_m (values depicted by the color bar). The central zero-bias peak suppressed in order to highlight the density at the outer ring using the envelope function $(1 - e^{-|\delta_{rs}|})$, where $|\delta_{rs}| = |\mathbf{r} - \mathbf{r}_s|$. Outside the shaded gray region, the spin texture flattens out (up to $10^{-5} m_z^{\text{center}}$). The peaks corresponding to the ring structure lie outside the shaded region and remain pinned at the same location with increasing decay length until $\xi_m \leq 8$ and begin to diverge thereafter due to edge effects. (d) LDOS at different values of exchange coupling m_0 (with $\xi_m = 1$). The plot shows a diagonal cross section of the LDOS at zero energy with the central zero-bias peak suppressed. (e) Representative 2D zero-energy LDOS plots are shown at magnetic vortex decay lengths, $\xi_m = (3, 5, 8)$ with fixed $m_0 = -0.35$. (f) Representative 2D zero-energy LDOS plots are shown at magnetic vortex decay lengths, $m_0 = (-0.36, -0.39, -0.42)$ with fixed $\xi_m = 1$. Radius R_{hv} calculated from Eq. (23) is shown by dotted black circles in (e) and (f). Parameters: $L = 75$, $\Delta = 0.3$, $\varphi = 0$, $u = 0.6$, $\mu = 0$, and $t = 1$.

vortex core. In Fig. 3(e) we observe a clear zero-bias peak in the local density of states. Importantly, this peak has *evolved continuously* from the Majorana zero mode present in the pure SC vortex. By adiabatic continuity we thus conclude that it must represent a Majorana mode. The contribution to the zero-bias peak is entirely sourced from spin-up sector—reflecting the polarization of the superconductor electrons by the spin vortex.

In addition to the localized Majorana mode at the core of the hybrid vortex, we observe in Fig. 3(f) a ring surrounding the vortex core. It is natural to interpret this feature as marking the boundary between the inner topological region and the outer trivial region. We may also expect it to contain the second Majorana zero mode that was previously localized at the system outer boundary. This identification is confirmed by a decoupling procedure detailed in Appendix A 2 which allows one to disentangle wave functions belonging to two weakly coupled MZMs. Plotting the decoupled MZM wave functions in Figs. 3(g) and 3(h) indeed shows that the two Majorana modes are localized at the vortex core and at the ring, respectively. This procedure also provides a sharp distinction between a pair of MZMs weakly split in energy by their wave-function overlap and a pair of ordinary CdGM

states—the latter would be *both* localized at the vortex core. It is a unique characteristic of MZMs that they can be spatially separated to an arbitrary distance, a property that also underlies their ability to encode quantum information in a way that is inaccessible to environmental decoherence [4].

We can estimate the radius R_{hv} of the ring by comparing it with the radius at which the local excitation gap vanishes. The local excitation gap for the hybrid vortex [see Eq. (B6)] includes contributions from the gradients of the phase of both the superconducting and the magnetic vortex which modifies the expression for the local excitation gap given in Eq. (22), as discussed and derived in Appendix B. For the hybrid vortex system, we find

$$R_{\text{hv}}^{\text{eqn}} = \frac{2u}{||m_0| - \Delta_0|}. \quad (23)$$

This analytical expression of the critical radius again coincides with the radius of the ring from the LDOS numerical simulations.

Majorana zero modes are present at the core of the hybrid vortex for a range of parameters as demonstrated in Figs. 4(a) and 4(b). Here we observe a prominent zero-bias peak in the LDOS that is robust for different values of the decay length,

ξ_m , which controls the size of the magnetic vortex. We also find the critical value of magnitude of the exchange coupling parameter, m_0 , below which the zero-bias peak splits (≈ 0.33 for the chosen parameters and magnetic vortex profile).

To study the spatial features of the Majorana modes present in the hybrid vortex, we plot the LDOS at zero energy across a diagonal cross section of the lattice for different decay lengths of the magnetic vortex in Fig. 4(c). The value of R_{hv} is much larger than the radius at which the spin texture flattens out with m_z nearly zero ($m_z \sim 10^{-5} m_z^{\text{core}}$). Further, we observe that there is no significant difference in the location of the peaks corresponding to the outer ring on variation of ξ_m . This further supports our interpretation of the topological phase as being enabled by the orbital magnetic effect through the emergent vector potential \mathcal{A} introduced in the previous subsection.

Now we look at the spatial features of zero-energy LDOS while varying the magnitude of the exchange coupling m_0 at fixed value of ξ_m plotted in Fig. 4(d). The vortex core Majorana state persists for the entire range of parameters shown in Fig. 4(d). The radius of the outer ring, apparent in the LDOS, decreases with the increase in exchange coupling strength. This decrease in the radius of the topological region is expected from the analytical estimate given in Eq. (23). We finally note that at larger magnitude of m_0 , the wave function corresponding to outer Majorana mode can exhibit delocalization in the region between the ring and the edge of the system. We attribute this to the relatively small gap size in the outer region as illustrated further in Fig. 8 of Appendix B, which implies long SC coherence length in this region.

C. Supercurrents

To understand the characteristic features of hybrid vortices, we study the local supercurrents in these systems. As derived in Appendix A3, supercurrent flowing along the bond connecting sites \mathbf{r} and \mathbf{r}' is given by

$$J_{ij} = -\frac{ie}{\hbar} \sum_{\sigma, \sigma'} \left[\sum_n h_{i\sigma, j\sigma'} u_{i\sigma}^n u_{j\sigma'}^{n*} f(E_n) - \text{c.c.} \right], \quad (24)$$

where we denote the matrix element between site i (spin σ) and site j (spin σ') as $h_{i\sigma, j\sigma'}$. We denote the bond current from x to $x+1$ on the lattice as J_x and that from y to $y+1$ as J_y . The local supercurrent vector is then given by $\mathbf{J}_{xy} = (J_x, J_y)$.

To understand the origin of this supercurrent analytically, let us revisit Eq. (20) where we incorporated the in-plane magnetization into the magnetic vector potential $\alpha\mathcal{A} = (m_y, -m_x, 0)$. The supercurrent density is generally given by

$$\mathbf{j}(\mathbf{r}) = n_s(\nabla\theta_s - 2\mathcal{A}), \quad (25)$$

where n_s denotes the superfluid density. In the self-consistent solution the phase field $\theta_s(\mathbf{r})$ will adjust to minimize the free-energy cost of the current, $\sim(\nabla\theta_s - 2\mathcal{A})^2$. Because $\nabla \times \nabla\theta_s = 0$, except for isolated points (vortices), only the longitudinal part of \mathcal{A} can be screened completely; the transverse part, corresponding to nonzero field \mathcal{B} , can only be screened partially by incorporating vortices into the phase field. More details on this and a relevant calculation are provided in Appendix C. We know from Eq. (21) that $|\mathcal{B}| \propto$

$\cos\varphi$, implying that supercurrents should decrease as the helicity parameter increases from 0, eventually vanishing as $\varphi \rightarrow \pi/2$ and \mathcal{A} becomes purely longitudinal. This expectation is indeed borne out in the microscopic calculation of the supercurrent displayed in Fig. 5 for several values of the helicity parameter. An interesting feature of the current flow is its constant magnitude independent of the radius r . This is to be contrasted with a regular Abrikosov vortex where the magnitude decays as $|\nabla\theta_s| \sim 1/r$. This peculiar behavior can be traced back to the fact that the current here is proportional to the magnetization field of the magnetic vortex which itself retains a constant magnitude independent of r .

In a hybrid vortex we expect the usual vortex current pattern with the amplitude decaying as $1/r$ to be superimposed on the anomalous current distribution shown in Fig. 5. For different values of magnetic vortex decay lengths ξ_m this is displayed in Figs. 6(a)–6(d). The case where $\xi_m \rightarrow \infty$, shown in Fig. 6(a), corresponds to a pure superconducting vortex subject to an external Zeeman field, m_z . The supercurrents now flow counterclockwise and follow the expected $1/r$ behavior outside the vortex core. For finite decay lengths, the hybrid vortex exhibits clockwise supercurrents away from the core while closer to the core the currents are counterclockwise. This can be understood as a competition between the $1/r$ Abrikosov contribution and the r -independent magnetization contribution. The former partially cancels the latter at intermediate distances, thus lowering the free-energy cost of the hybrid vortex compared to the pure magnetic vortex. This cancellation also provides some intuition behind the notion of stability of the hybrid vortex. Another interesting feature to note is the presence of the outer ringlike structure in the magnitude of the supercurrents. The outer edge of these supercurrent rings also correspond to the ring in the LDOS observed earlier in Fig. 4.

We perform a similar analysis for the local supercurrents with varying exchange coupling parameter, m_0 , and plot the results in Figs. 6(e)–6(h). As before, we observe the clockwise supercurrent flow away from the core of the vortex. Closer to the vortex core, we expect the supercurrents to reverse the direction. Note that in the representative plots shown in Figs. 6(e)–6(h), the reversal of the supercurrent is not immediately evident owing to the fact that magnetic and the superconducting vortex are approximately of the same size. Here again, we see a prominent outer ring in the magnitude of the supercurrents. The radius of this outer ring decreases with increasing magnitude of the exchange coupling, similarly to the outer ring in the LDOS plots Fig. 4.

IV. DISCUSSION

We performed a study of a novel “hybrid” vortex comprising a superconducting and magnetic vortex. Such a composite can occur in a quasi-2D heterostructure formed by a thin easy-plane ferromagnet and a superconductor with Rashba spin-orbit coupling. The magnetic and superconducting vortices present in this composite structure can form an energetically favorable hybrid vortex. We showed this analytically by considering the magneto-electric interaction induced by the spin-orbit coupling as well as by detailed numerical simulations of a minimal microscopic model.

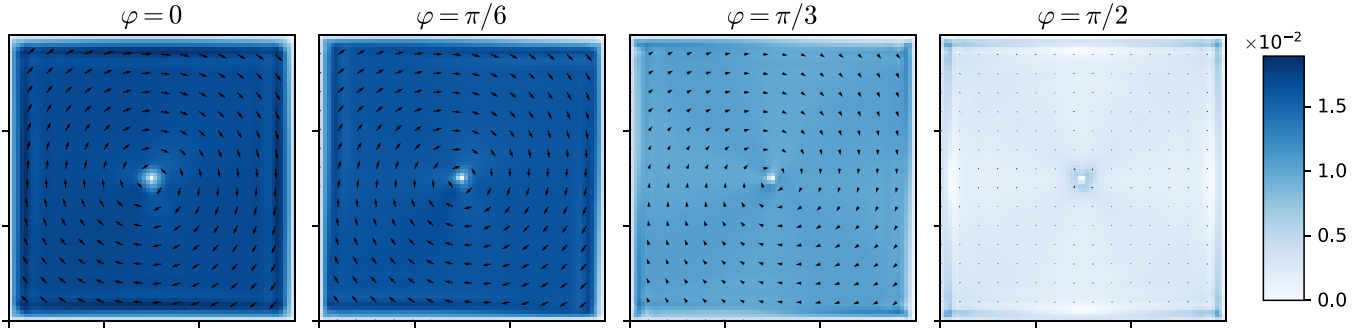


FIG. 5. Supercurrents in a system with uniform superconducting order parameter and a magnetic vortex with helicities $\varphi = (0, \frac{\pi}{6}, \frac{\pi}{3}, \frac{\pi}{2})$. The phase of the superconducting order parameter is given by Eq. (C2). Parameters: $L = 75$, $\Delta = 0.3$, $m_0 = -0.3$, $\xi_s = \xi_m = 1$, $u = 0.6$, $\mu = 0$, and $t = 1$.

We established the presence of zero-energy Majorana bound states in the hybrid vortex by appealing to adiabatic continuity arguments. Using the characteristic zero-bias peak in the local density of states, we studied the features of these Majorana modes. In addition to the Majorana zero mode localized at the core of the hybrid vortex, we also observed its partner zero mode localized in the ringlike structure surrounding the hybrid vortex. The ring demarcates a disk-shaped topological region centered at the vortex core. Remarkably, the topological phase inside the ring is stabilized not by an out of plane magnetization m_z , as would be the case in conventional models, but by an emergent orbital magnetic field. This emergent orbital magnetic field arises from the magnetization

field of the spin vortex which couples as vector potential to electrons in the superconductor. We derived an estimate for the ring radius using the emergent magnetic field hypothesis and found that it agrees quantitatively with our numerical results. We also studied the dependence of the topological ring radius on the helicity of the magnetic vortex which likewise supports the physical picture that we presented.

The superflow pattern around the hybrid vortex shows an unusual behavior in that the supercurrent generically reverses its direction at some intermediate radius. This can be understood as a competition between the usual Abrikosov vortex superflow that decays as $1/r$ and an anomalous magnetization-induced current that is r independent. This par-

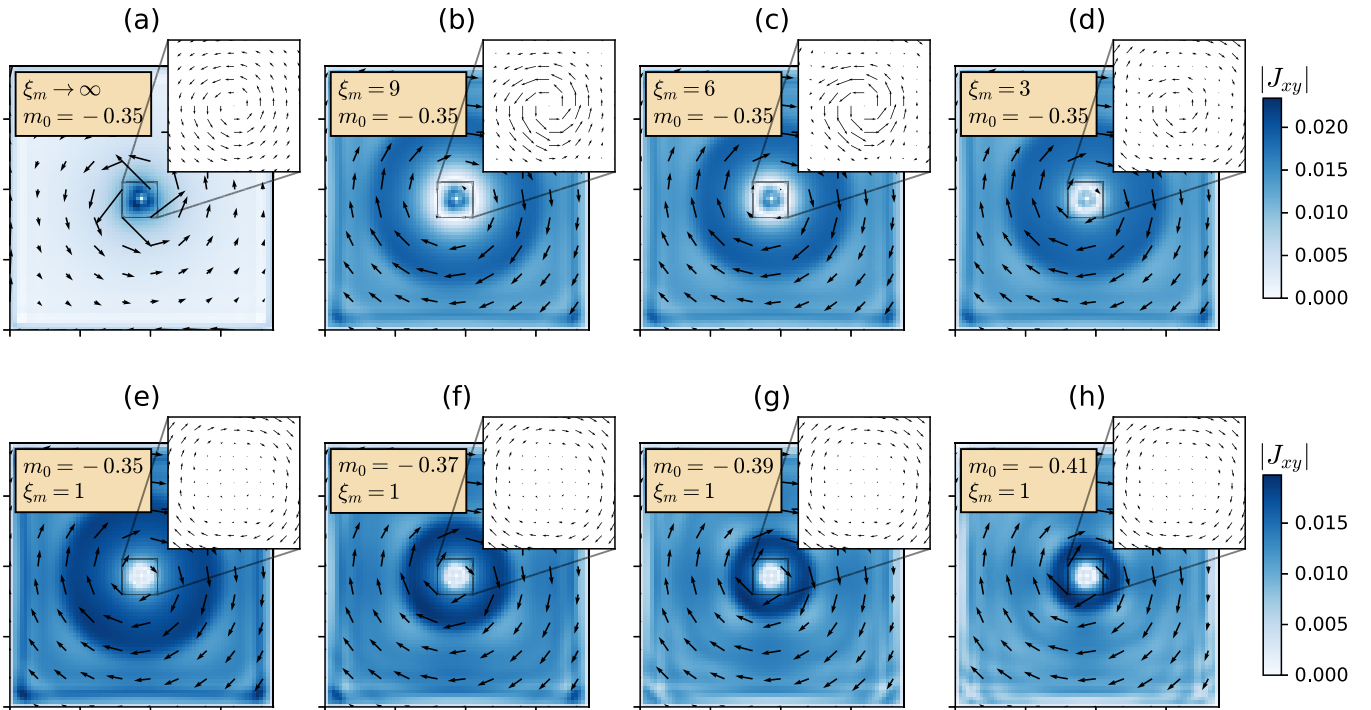


FIG. 6. [(a)–(d)] Local supercurrents plotted for different values of magnetic vortex decay lengths, $\xi_m = (\infty, 9, 6, 3)$. Case (a) corresponds to a system with superconducting vortex and uniform Zeeman field. [(e)–(h)] Local supercurrents plotted for exchange coupling strengths, $m_0 = (-0.35, -0.37, -0.39, -0.41)$. The vectors (arrows) correspond to the direction of the flow of the supercurrent given by the vector \mathbf{J}_{xy} . The color bars represent the magnitude of J_{xy} . The insets show the orientation of the local supercurrents around the vortex core. Parameters: $L = 75$, $\Delta = 0.3$, $\xi_s = \xi_m = 1$, $\varphi = 0$, $u = 0.6$, $\mu = 0$, and $t = 1$.

tial cancellation of the net current near the reversal region also provides intuition for the energetic stability of the hybrid vortex.

As future avenues of research, the theory for single hybrid vortex can be extended to multiple hybrid vortices. For instance, the energetics in the two hybrid vortices would now need to account for the repulsion between two magnetic vortices in addition to the attraction between the superconducting and magnetic vortices of different pairs. This makes the extension to multiple hybrid vortices an interesting problem. Additionally, a detailed analysis of the Majorana modes with the helicity of the magnetic vortex would be very useful in further understanding the Majorana modes in hybrid vortices.

Last, we note that the techniques developed here to investigate the topological phase of the hybrid vortex are also more broadly applicable to systems where superconductivity and ferromagnetism can coexist. An example of this is the iron-based superconductor $\text{FeTe}_{1-x}\text{Se}_x$, where topological superconductivity [44] has been established with recent experimental [45–47] and theoretical [48–51] evidence supporting the existence Majorana modes in vortices. Such systems exhibiting complex interplay among topology, magnetism, and superconductivity are of burgeoning interest in device technology.

ACKNOWLEDGMENTS

We thank O. Can, R. Haenel, T. Tummuru, and B. Zhou for helpful discussions. This research was supported in part by NSERC and the Canada First Research Excellence Fund, Quantum Materials and Future Technologies Program. S.D. is additionally supported by the Japan Society for the Promotion of Science KAKENHI (Grant No. JP19H01808).

APPENDIX A: DETAILS OF THE NUMERICS

1. Local density of states

Consider the particle number operator on site i given by $N_i = \sum_{\sigma} N_{i\sigma}$ with $N_{i\sigma} = c_{i\sigma}^{\dagger} c_{i\sigma}$. The eigenvector at energy E_n after diagonalization of the BdG Hamiltonian assumes the form $\psi_{i,n} = (u_{i\uparrow}, u_{i\downarrow}, v_{i\downarrow}, -v_{i\uparrow})^T$. Using the symmetries of the BdG Hamiltonian, we can also write the number operators as

$$N_{i\sigma} = \sum_n |u_{i\sigma}^n|^2 f(E_n) = \sum_n |v_{i\sigma}^n|^2 [1 - f(E_n)], \quad (\text{A1})$$

where $f(E_n)$ is the Fermi-Dirac distribution function.

The probability distribution of the particle wave function at site i with energy $E_n > 0$ is evaluated as $|\psi_{pi}^n|^2 = \sum_{\sigma} |u_{i\sigma}^n|^2$. The local density of states is given by

$$\rho_{i\sigma}(E) = \sum_n' [|u_{i\sigma}^n|^2 \delta(E_n - E) + |v_{i\sigma}^n|^2 \delta(E_n + E)]. \quad (\text{A2})$$

2. Majorana wave functions

The Majorana modes, if present, will manifest themselves as zero-energy peaks in the local density of states. Majorana modes always come in pairs [3] and, in a finite-size system, there will always be a small energy splitting due to their wave-

function overlap. Because of this, in the context of the vortex core states, it may be difficult to distinguish such weakly split Majorana modes from the ordinary CdGM modes [35] based purely on their energy spectra. As we explain below a sharp distinction between the two types of states can nevertheless be drawn based on the structure of their corresponding eigenstates.

We first assume two near-zero modes to be a linear superposition of two Majorana wave functions localized at the core of the vortex and the edge of the topological region, respectively. If we denote the Majorana mode creation operators as γ_c and γ_e , then the Hamiltonian for the small overlap of the wave functions is uniquely defined by their self-conjugation property $\gamma = \gamma^{\dagger}$ as follows:

$$h_{\text{eff}} = i\epsilon_0 \gamma_c \gamma_e = \frac{\epsilon_0}{2} \Gamma^{\dagger} \sigma^y \Gamma, \quad (\text{A3})$$

where $\Gamma = (\gamma_c, \gamma_e)^T$. The above equation implies that the wave functions ϕ^{\pm} corresponding to the eigenvalues of $\pm\epsilon_0$ are related to the zero mode wave functions as $\phi^{\pm} = \frac{1}{\sqrt{2}}(\phi_c \pm \phi_e)$. Inverting this relation then gives the decoupled Majorana modes localized at the vortex core and edge of the topological region, respectively. Crucially, we note that this type of decoupling procedure applied to a pair of ordinary CdGM states at opposite energies will yield two states with wave functions *both* localized in the vortex core.

For the hybrid vortex discussed in Sec. III B, the local density of states at the core [Fig. 3(e)] exhibits a prominent peak near zero energy. The wave functions corresponding to the two near-zero modes are decoupled according to the procedure outlined above and the corresponding amplitudes $|\phi_{c/e}|^2$ are plotted in Fig. 7. The amplitudes show clear spatial separation with $|\phi_c|^2$ and $|\phi_e|^2$ supported at the core and the ring, respectively, as expected of a pair of Majorana modes. By contrast, the higher-energy states do not show such separation and are identified as CdGM modes.

The particle-hole symmetry of the BdG Hamiltonian furthermore implies that a Majorana mode at zero energy must also be an eigenstate of the charge conjugation operator [3]. As a result the individual components of the Majorana wave function satisfy the relations $u_{\uparrow} = c^* v_{\uparrow}^*$ and $u_{\downarrow} = c^* v_{\downarrow}^*$ where $|c| = 1$. These conditions can be observed in Fig. 7 where we plot the spatial distribution of the decoupled Majorana wave-function amplitudes $|\phi_c|^2$ and $|\phi_e|^2$ as a function of the distance from vortex center. This again is to be contrasted with the behavior of ordinary CdGM states (ϵ_1) in Fig. 7 by observing that all the components of such non-Majorana wave function are independent, i.e., $|u_{\uparrow}|^2 \neq |v_{\uparrow}|^2$ and $|u_{\downarrow}|^2 \neq |v_{\downarrow}|^2$. Further, the spin-polarization of the decoupled Majorana wave functions is evident in Fig. 7.

3. Local supercurrents

To calculate the local supercurrents we begin with the Heisenberg equation of motion for particle at lattice site i ,

$$i\hbar \frac{\partial \langle N_i \rangle}{\partial t} = \langle [N_i, H] \rangle, \quad (\text{A4})$$

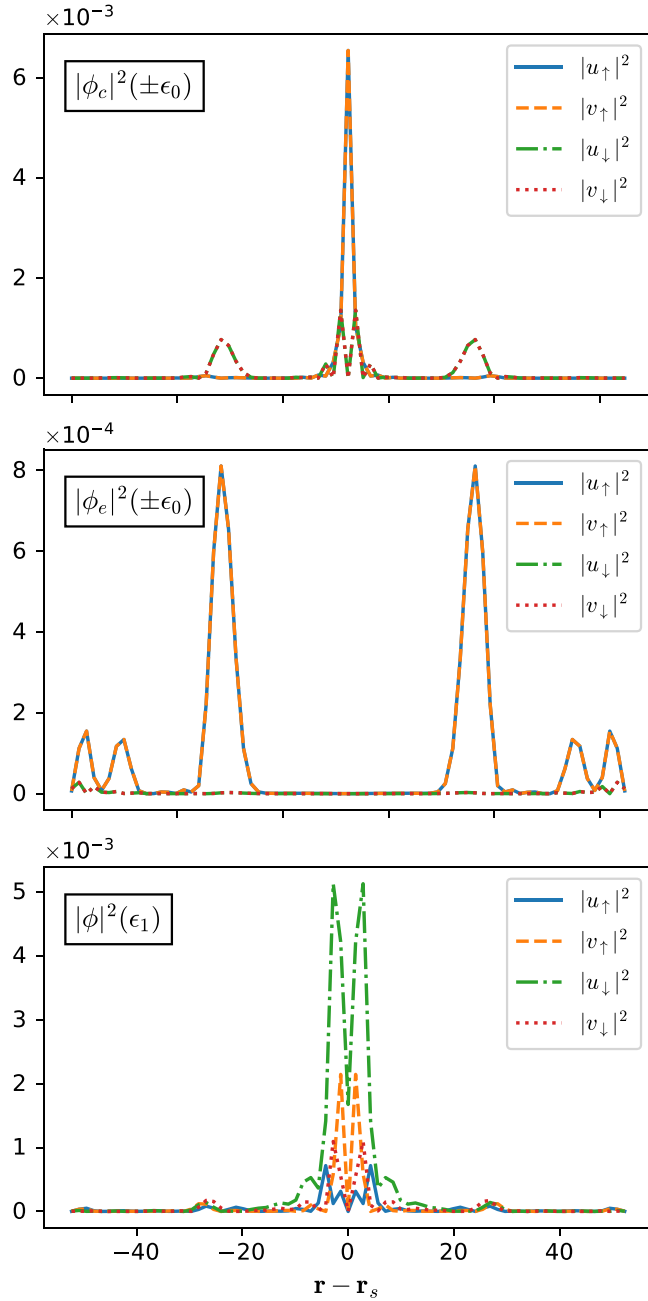


FIG. 7. Spatial distribution of the decoupled Majorana wave functions $\phi_{e/c}$ and the ordinary CdGM wave functions (energy ϵ_1) as a function of distance from the hybrid vortex core. The CdGM state corresponds to a dominant nonzero energy peak at $\epsilon_1 = 0.14\Delta$ in the LDOS shown in Fig. 3(e). Here the system parameters are the same as those in Figs. 3(e)–3(h) of the main text.

where H is the tight-binding Hamiltonian. Denoting its matrix element between site i (spin σ) and site j (spin σ') as $h_{i\sigma, j\sigma'}$, we can rewrite the Heisenberg equation of motion as follows:

$$i\hbar \frac{\partial \langle N_i \rangle}{\partial t} = \left\langle \sum_{\substack{j \neq i \\ \sigma, \sigma'}} (h_{i\sigma, j\sigma'} c_{i\sigma}^\dagger c_{j\sigma'} - h_{j\sigma', i\sigma} c_{j\sigma'}^\dagger c_{i\sigma}) \right\rangle. \quad (\text{A5})$$

Using the above relation, the current operator from site j to site i is

$$\hat{J}_{ij} = -\frac{ie}{\hbar} \sum_{\sigma, \sigma'} (h_{i\sigma, j\sigma'} c_{i\sigma}^\dagger c_{j\sigma'} - h_{j\sigma', i\sigma} c_{j\sigma'}^\dagger c_{i\sigma}). \quad (\text{A6})$$

The average bond current is given by taking the expectation value of the current operator with the ground-state eigenvectors (for a superconductor, the ground-state eigenvectors are given by summing over all negative energies),

$$J_{ij} = -\frac{ie}{\hbar} \sum_{\sigma, \sigma'} h_{i\sigma, j\sigma'} \sum_n' \{ u_{i\sigma}^n u_{j\sigma'}^{n*} f(E_n) + \sigma \sigma^* v_{i\sigma}^n v_{j\sigma'}^{n*} [1 - f(E_n)] - \text{c.c.} \}. \quad (\text{A7})$$

Using the symmetries of the BdG Hamiltonian [see Eq. (A1)], the equation of bond current can be simplified to

$$J_{ij} = -\frac{ie}{\hbar} \sum_{\sigma, \sigma'} \left[\sum_h h_{i\sigma, j\sigma'} u_{i\sigma}^n u_{j\sigma'}^{n*} f(E_n) - \text{c.c.} \right]. \quad (\text{A8})$$

APPENDIX B: TOPOLOGICAL REGION OF THE HYBRID VORTEX SYSTEM

We consider energy spectra in the vicinity of a pure magnetic and a hybrid vortex using a semiclassical approximation with the goal of understanding the apparent gap closing outside the core observed in our numerical simulations. Away from the vortex core, near-zero momenta at $\mu = 0$, this is described by the Hamiltonian in Eq. (19). We assume that away from the vortex core, the spins of the ferromagnet are entirely in the xy plane, making the magnetic texture $\mathbf{m} = m_0(\cos \phi_m, \sin \phi_m, 0)$. Superfluid velocity in a superconducting vortex is defined as $\mathbf{v}_s = \nabla \theta_s = \frac{1}{r} \hat{\phi}$. Similarly, here we define the magnetic vortex phase gradient as $\mathbf{v}_m = \nabla \phi_m = \frac{1}{r} \hat{\phi}$.

We begin with a pure magnetic vortex. Squaring the Hamiltonian in Eq. (19) and systematically neglecting terms containing p^2 results in

$$H^2 = \Delta_0^2 + m_0^2 + 2\Delta_0 m_0 (\mathbf{m} \cdot \boldsymbol{\sigma}) \tau_x + m_0 \{ \alpha (\boldsymbol{\sigma} \times \mathbf{p})_z, (\mathbf{m} \cdot \boldsymbol{\sigma}) \} \tau_z, \quad (\text{B1})$$

where the the anticommutator is defined as $\{A, B\} = AB + BA$. Reshuffling the constant terms and squaring once again using the same assumptions as before, we find

$$\begin{aligned} & (H^2 - \Delta_0^2 - m_0^2)^2 \\ &= 4\Delta_0^2 m_0^2 + m_0^2 \{ \alpha (\boldsymbol{\sigma} \times \mathbf{p})_z, (\mathbf{m} \cdot \boldsymbol{\sigma}) \}^2 \\ &+ m_0^2 \{ 2\Delta_0 (\mathbf{m} \cdot \boldsymbol{\sigma}) \tau_x, \alpha (\boldsymbol{\sigma} \times \mathbf{p})_z, (\mathbf{m} \cdot \boldsymbol{\sigma}) \} \tau_z. \end{aligned} \quad (\text{B2})$$

The anticommutators in the above equation can be solved by identifying $\mathbf{p} = -i\nabla$ and by considering all spatially dependent functions to be slowly varying such that the second derivatives are negligible,

$$m_0^2 \{ \alpha (\boldsymbol{\sigma} \times \mathbf{p})_z, (\mathbf{m} \cdot \boldsymbol{\sigma}) \}^2 = \alpha^2 m_0^2 v_m^2, \quad (\text{B3})$$

$$\{ 2\Delta_0 (\mathbf{m} \cdot \boldsymbol{\sigma}) \tau_x, \alpha (\boldsymbol{\sigma} \times \mathbf{p})_z, (\mathbf{m} \cdot \boldsymbol{\sigma}) \} \tau_z = 0. \quad (\text{B4})$$

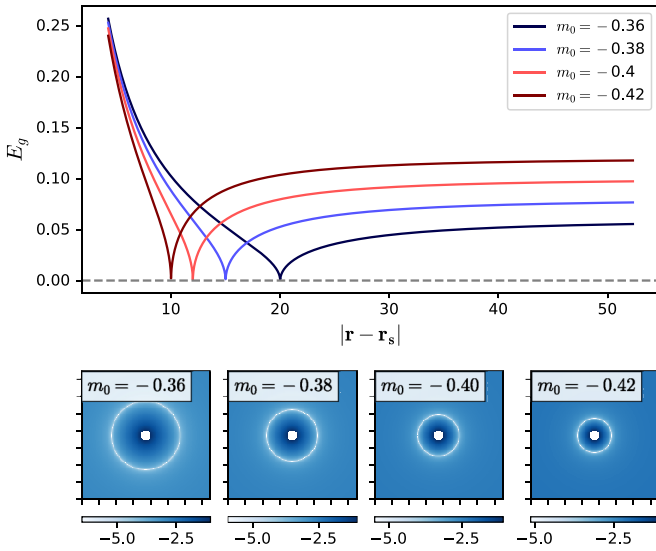


FIG. 8. Top: Energy gap E_g from Eq. (B6) for the hybrid vortex as a function of the distance from the core. Vanishing E_g defines the critical radius R_{hv} which is dependent on m_0 . Bottom: $\log(E_g)$ plotted for representative values of m_0 to illustrate the disk shaped topological region of radius R_{hv} . Parameters: $L = 75$, $\Delta = 0.3$, $\xi_s = \xi_m = 1$, $\varphi = 0$, $u = 0.6$, $\mu = 0$, and $t = 1$.

Solving for the eigenvalues gives

$$E_g^2 = \left| \Delta_0^2 + m_0^2 \pm 2\sqrt{\Delta_0^2 m_0^2 + u^2 m_0^2 v_m^2} \right|, \quad (\text{B5})$$

where $u = \frac{\alpha}{2a}$ and $v_m^2 = \frac{1}{r^2}$ as defined previously. We set the lattice constant $a = 1$. As the minus sign clearly corresponds to a lower energy it will represent the local energy gap. This, along with identifying $m_0^2 v_m^2 = \mathcal{B}^2$, leads to Eq. (22) in the main text. The disk-shaped topologically nontrivial region surrounding the vortex core extends up to a radius R_{mv} where $E_g = 0$.

A similar procedure gives the energy gap for the hybrid vortex where the additional terms arise from the spatial dependence of the phase of the superconducting order parameter. We find

$$E_g^2 = \left| \Delta_0^2 + m_0^2 - 2\sqrt{\Delta_0^2 m_0^2 + u^2 (m_0 v_m + \Delta_0 v_s)^2} \right|. \quad (\text{B6})$$

We plot E_g in Fig. 8 where we show that the system is gapped on either side of R_{hv} defined by the condition $E_g = 0$ and given in Eq. (23). In Fig. 9 we compare it to the ring radius obtained in the numerical simulations.

While Eq. (23) suggests a divergence at $|m_0| = \Delta_0$, we note here that the topological region exists only when $|m_0|$ is above a critical value which is always greater than Δ_0 . This is also discussed in Sec. III B (Fig. 4) where we show the splitting of Majorana zero-bias peak below a critical value, $|m_0| \leq 0.33$, for $\Delta = 0.3$.

APPENDIX C: SUPERCURRENTS IN A PURE MAGNETIC VORTEX

To the first order in SOC, the supercurrent is given by [19],

$$\mathbf{j}(\mathbf{r}) = \frac{n_s}{2m} \nabla \theta_s + \alpha (\hat{\mathbf{z}} \times \mathbf{m}). \quad (\text{C1})$$

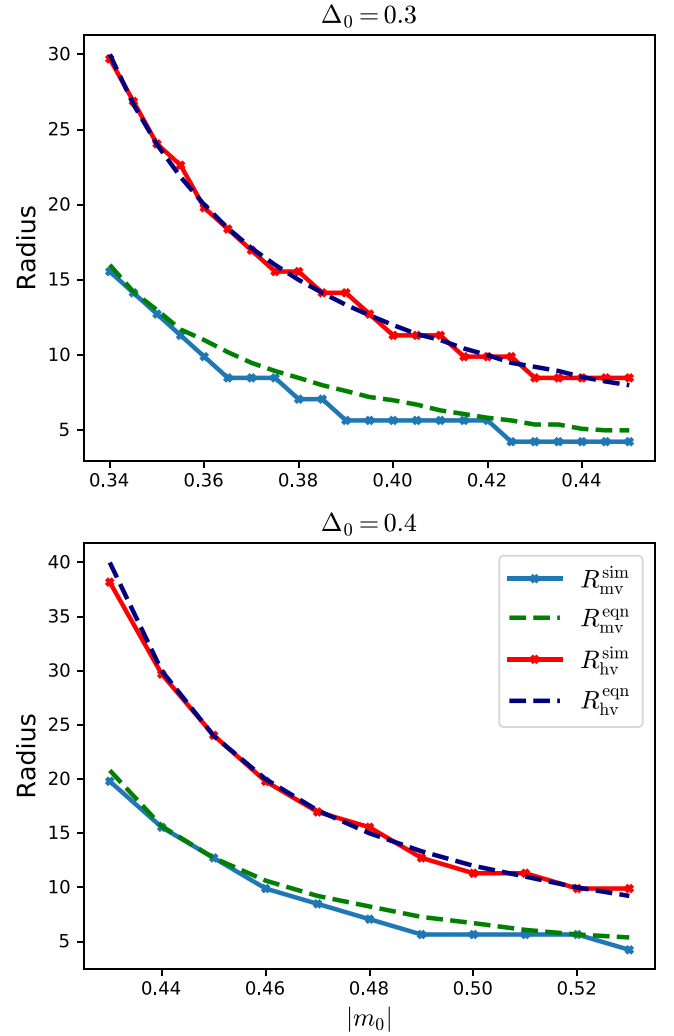


FIG. 9. The plot shows the radius of the topological region of the magnetic vortex (R_{mv}^{eqn}) given by Eq. (22) as a function of the exchange coupling parameter and compares it to the radius of the ring obtained by simulations (R_{mv}^{sim}) for $\Delta_0 = 0.3$ (top panel) and $\Delta_0 = 0.4$ (bottom panel). The plot also compares the radius of the topological region around the hybrid vortex (R_{hv}^{eqn}) calculated from Eq. (B6) and the radius of the ring around the hybrid vortex obtained from the simulations (R_{hv}^{sim}).

On imposing continuity, $\nabla \cdot \mathbf{j} = 0$, the solution of the superconducting phase, as derived by Pershoguba *et al.* [19], is given by

$$\theta_s = \frac{m\alpha}{n_s} \mathbf{r} \cdot (\mathbf{m} \times \hat{\mathbf{z}}). \quad (\text{C2})$$

For our system, $m = 1$ and $n_s = 1$. To obtain the supercurrents for a pure magnetic vortex shown in Fig. 5, we include the phase, θ_s , from Eq. (C2) in the superconducting order parameter.

We note here that a pure magnetic vortex can by itself induce a topological phase transition in the superconductor since it has a non-co-planar spin ordering Nakosai *et al.* [14]. In our case when the magnitude of the exchange coupling is increased beyond a critical value we see this transition. The signature of the phase transition can be observed in the

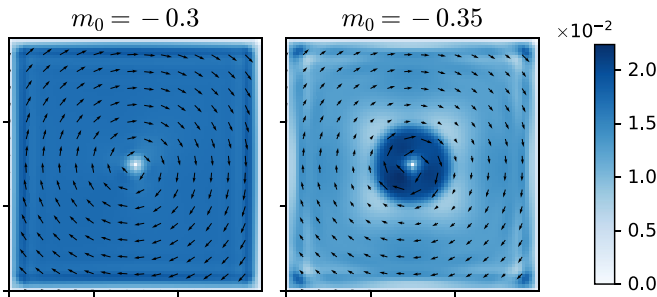


FIG. 10. Supercurrents for a pure magnetic vortex in the trivial phase (left) and the topological phase (right). The topological phase transition occurs at the critical exchange coupling $|m_0| \approx 0.33$ when $\Delta = 0.3$ for the chosen parameters. The phase of the superconducting order parameter is given by Eq. (C2).

supercurrents as we tune m_0 . Above a certain value the supercurrents are no longer uniform throughout the system as expected from (C1), a clear ring forms separating an inner topologically non trivial region including the vortex core. This is shown in Fig. 10 for $\varphi = 0$.

APPENDIX D: MODIFIED ELECTROMAGNETIC DUALITY

The theory for the planar ferromagnet can be cast into a dual theory of electromagnetism in $2 + 1$ dimensions with magnons acting as the single photon and vortices acting as

electric charges carrying magnetic fluxes [33,52]. The duality transformation is between the Lagrangian densities:

$$S(\cos \Theta - 1)\dot{\Phi} - \frac{\tilde{A}}{2}(\nabla\Phi)^2 - \frac{\mathcal{K}}{2}\cos^2\Theta \Rightarrow -2\pi J^\mu \tilde{A}_\mu - \frac{F^{\mu\nu}F_{\mu\nu}}{e^2}. \quad (\text{D1})$$

In the spin Lagrangian S is the spin density \tilde{A} is proportional to Heisenberg exchange and \mathcal{K}_a is the easy plane anisotropy, in the electromagnetic Lagrangian $e^2 = S\tilde{A}/\mathcal{K}_a$. This duality mapping has two parts, the conserved Noether current conjugate to the field Φ (magnetic spin current \mathbf{J}_m) which is mapped through a Bianchi identity to the gauge field A and the electromagnetic tensor. The second part is the matter current J which consists of electrical charges (magnetic vortices [52]) which are also conserved due to their topology, and hence follow a continuity equation, for details see Dasgupta *et al.* [33]. A similar dual construction can be made with the superconducting phase, the conserved current there is the supercurrent, $\mathbf{J}_s \propto \nabla\theta_s$.

While this duality would have existed in our heterostructure for an interaction of the form $-\mathbf{J}_m \cdot \mathbf{J}_s$, the magnetoelectric interaction does not allow such a construction. This implies that the mapping to electrostatics no longer holds and treating the magnetic vortices and superconducting vortices as interacting charges is not possible.

-
- [1] J. Alicea, New directions in the pursuit of majorana fermions in solid state systems, *Rep. Prog. Phys.* **75**, 076501 (2012).
- [2] C. W. J. Beenakker, Search for majorana fermions in superconductors, *Annu. Rev. Condens. Matter Phys.* **4**, 113 (2013).
- [3] S. R. Elliott and M. Franz, Colloquium: Majorana fermions in nuclear, particle, and solid-state physics, *Rev. Mod. Phys.* **87**, 137 (2015).
- [4] C. Nayak, S. H. Simon, A. Stern, M. Freedman, and S. Das Sarma, Non-abelian anyons and topological quantum computation, *Rev. Mod. Phys.* **80**, 1083 (2008).
- [5] A. Y Kitaev, Unpaired majorana fermions in quantum wires, *Phys. Usp.* **44**, 131 (2001).
- [6] L. Fu and C. L. Kane, Superconducting Proximity Effect and Majorana Fermions at the Surface of a Topological Insulator, *Phys. Rev. Lett.* **100**, 096407 (2008).
- [7] R. M. Lutchyn, J. D. Sau, and S. Das Sarma, Majorana Fermions and a Topological Phase Transition in Semiconductor-Superconductor Heterostructures, *Phys. Rev. Lett.* **105**, 077001 (2010).
- [8] J. D. Sau, R. M. Lutchyn, S. Tewari, and S. Das Sarma, Generic New Platform for Topological Quantum Computation Using Semiconductor Heterostructures, *Phys. Rev. Lett.* **104**, 040502 (2010).
- [9] Y. Oreg, G. Refael, and F. von Oppen, Helical Liquids and Majorana Bound States in Quantum Wires, *Phys. Rev. Lett.* **105**, 177002 (2010).
- [10] T.-P. Choy, J. M. Edge, A. R. Akhmerov, and C. W. J. Beenakker, Majorana fermions emerging from magnetic nanoparticles on a superconductor without spin-orbit coupling, *Phys. Rev. B* **84**, 195442 (2011).
- [11] J. Klinovaja, P. Stano, A. Yazdani, and D. Loss, Topological Superconductivity and Majorana Fermions in RKKY Systems, *Phys. Rev. Lett.* **111**, 186805 (2013).
- [12] M. M. Vazifeh and M. Franz, Self-Organized Topological State with Majorana Fermions, *Phys. Rev. Lett.* **111**, 206802 (2013).
- [13] B. Braunecker and P. Simon, Interplay Between Classical Magnetic Moments and Superconductivity in Quantum One-Dimensional Conductors: Toward a Self-Sustained Topological Majorana Phase, *Phys. Rev. Lett.* **111**, 147202 (2013).
- [14] S. Nakosai, Y. Tanaka, and N. Nagaosa, Two-dimensional p -wave superconducting states with magnetic moments on a conventional s -wave superconductor, *Phys. Rev. B* **88**, 180503(R) (2013).
- [15] G. C. Ménard, S. Guissart, C. Brun, R. T. Leriche, M. Trif, F. Debontridder, D. Demaille, D. Roditchev, P. Simon, and T. Cren, Two-dimensional topological superconductivity in Pb/Co/Si(111), *Nat. Commun.* **8**, 2040 (2017).
- [16] G. C. Ménard, A. Mesaros, C. Brun, F. Debontridder, D. Roditchev, P. Simon, and T. Cren, Isolated pairs of Majorana zero modes in a disordered superconducting lead monolayer, *Nat. Commun.* **10**, 2587 (2019).
- [17] G. Yang, P. Stano, J. Klinovaja, and D. Loss, Majorana bound states in magnetic skyrmions, *Phys. Rev. B* **93**, 224505 (2016).
- [18] S. Rex, I. V. Gornyi, and A. D. Mirlin, Majorana bound states in magnetic skyrmions imposed onto a superconductor, *Phys. Rev. B* **100**, 064504 (2019).

- [19] S. S. Pershoguba, K. Björnson, A. M. Black-Schaffer, and A. V. Balatsky, Currents Induced by Magnetic Impurities in Superconductors with Spin-Orbit Coupling, *Phys. Rev. Lett.* **115**, 116602 (2015).
- [20] K. M. D. Hals, M. Schechter, and M. S. Rudner, Composite Topological Excitations in Ferromagnet-Superconductor Heterostructures, *Phys. Rev. Lett.* **117**, 017001 (2016).
- [21] M. Dupont, Y. O. Kvashnin, M. Shiranzadei, J. Fransson, N. Laflorencie, and A. Kantian, Monolayer CrCl₃ as an Ideal Test Bed for the Universality Classes of 2D Magnetism, *Phys. Rev. Lett.* **127**, 037204 (2021).
- [22] A. Bedoya-Pinto, J.-R. Ji, A. K. Pandeya, P. Gargiani, M. Valvidares, P. Sessi, J. M. Taylor, F. Radu, K. Chang, and S. S. P. Parkin, Intrinsic 2d-xy ferromagnetism in a van der Waals monolayer, *Science* **374**, 616 (2021).
- [23] X. Lu, R. Fei, L. Zhu, and L. Yang, Meron-like topological spin defects in monolayer CrCl₃, *Nat. Commun.* **11**, 4724 (2020).
- [24] M. A. McGuire, G. Clark, S. KC, W. M. Chance, G. E. Jellison, V. R. Cooper, X. Xu, and B. C. Sales, Magnetic behavior and spin-lattice coupling in cleavable van der Waals layered CrCl₃ crystals, *Phys. Rev. Mater.* **1**, 014001 (2017).
- [25] O. A. Tretiakov, D. Clarke, G.-W. Chern, Y. B. Bazaliy, and O. Tchernyshyov, Dynamics of Domain Walls in Magnetic Nanostrips, *Phys. Rev. Lett.* **100**, 127204 (2008).
- [26] G. S. D. Beach, C. Nistor, C. Knutson, M. Tsoi, and J. L. Erskine, Dynamics of field-driven domain-wall propagation in ferromagnetic nanowires, *Nat. Mater.* **4**, 741 (2005).
- [27] J. Liu and L. Balents, Anomalous Hall Effect and Topological Defects in Antiferromagnetic Weyl Semimetals: Mn₃Sn/Ge, *Phys. Rev. Lett.* **119**, 087202 (2017).
- [28] X. Li, C. Collignon, L. Xu, H. Zuo, A. Cavanna, U. Gennser, D. Mailly, B. Fauqué, L. Balents, Z. Zhu, and K. Behnia, Chiral domain walls of mn₃sn and their memory, *Nat. Commun.* **10**, 3021 (2019).
- [29] S. Dasgupta and O. Tchernyshyov, Theory of spin waves in a hexagonal antiferromagnet, *Phys. Rev. B* **102**, 144417 (2020).
- [30] S. Mühlbauer, B. Binz, F. Jonietz, C. Pfleiderer, A. Rosch, A. Neubauer, R. Georgii, and P. Böni, Skyrmion lattice in a chiral magnet, *Science* **323**, 915 (2009).
- [31] M. Hervé, B. Dupé, R. Lopes, M. Böttcher, M. D. Martins, T. Balashov, L. Gerhard, J. Sinova, and W. Wulfhekel, Stabilizing spin spirals and isolated skyrmions at low magnetic field exploiting vanishing magnetic anisotropy, *Nat. Commun.* **9**, 1015 (2018).
- [32] H. Nam, H. Chen, T. Liu, J. Kim, C. Zhang, J. Yong, T. R. Lemberger, P. A. Kratz, J. R. Kirtley, K. Moler, P. W. Adams, A. H. MacDonald, and C.-K. Shih, Ultrathin two-dimensional superconductivity with strong spin-orbit coupling, *Proc. Natl. Acad. Sci. USA* **113**, 10513 (2016).
- [33] S. Dasgupta, S. Zhang, I. Bah, and O. Tchernyshyov, Quantum Statistics of Vortices from a Dual Theory of the xy Ferromagnet, *Phys. Rev. Lett.* **124**, 157203 (2020).
- [34] J. Pearl, Current distribution in superconducting films carrying quantized fluxoids, *Appl. Phys. Lett.* **5**, 65 (1964).
- [35] C. Caroli, P. G. De Gennes, and J. Matricon, Bound fermion states on a vortex line in a type II superconductor, *Phys. Lett.* **9**, 307 (1964).
- [36] A. I. Gubin, K. S. Il'in, S. A. Vitusevich, M. Siegel, and N. Klein, Dependence of magnetic penetration depth on the thickness of superconducting NB thin films, *Phys. Rev. B* **72**, 064503 (2005).
- [37] A. A. Thiele, Steady-State Motion of Magnetic Domains, *Phys. Rev. Lett.* **30**, 230 (1973).
- [38] D. L. Huber, Dynamics of spin vortices in two-dimensional planar magnets, *Phys. Rev. B* **26**, 3758 (1982).
- [39] J.-Y. Chauléau, R. Weil, A. Thiaville, and J. Miltat, Magnetic domain walls displacement: Automotion versus spin-transfer torque, *Phys. Rev. B* **82**, 214414 (2010).
- [40] S. Dasgupta and O. Tchernyshyov, Energy-momentum tensor of a ferromagnet, *Phys. Rev. B* **98**, 224401 (2018).
- [41] S. K. Kim, R. Myers, and Y. Tserkovnyak, Nonlocal Spin Transport Mediated by a Vortex Liquid in Superconductors, *Phys. Rev. Lett.* **121**, 187203 (2018).
- [42] G. E. Volovik, Fermion zero modes on vortices in chiral superconductors, *J. Exp. Theor. Phys. Lett.* **70**, 609 (1999).
- [43] M. Cheng, R. M. Lutchyn, V. Galitski, and S. Das Sarma, Tunneling of anyonic majorana excitations in topological superconductors, *Phys. Rev. B* **82**, 094504 (2010).
- [44] P. Zhang, K. Yaji, T. Hashimoto, Y. Ota, T. Kondo, K. Okazaki, Z. Wang, J. Wen, G. D. Gu, H. Ding, and S. Shin, Observation of topological superconductivity on the surface of an iron-based superconductor, *Science* **360**, 182 (2018).
- [45] D. Wang, L. Kong, P. Fan, H. Chen, S. Zhu, W. Liu, L. Cao, Y. Sun, S. Du, J. Schneeloch, R. Zhong, G. Gu, L. Fu, H. Ding, and H.-J. Gao, Evidence for majorana bound states in an iron-based superconductor, *Science* **362**, 333 (2018).
- [46] T. Machida, Y. Sun, S. Pyon, S. Takeda, Y. Kohsaka, T. Hanaguri, T. Sasagawa, and T. Tamegai, Zero-energy vortex bound state in the superconducting topological surface state of Fe(Se,Te), *Nat. Mater.* **18**, 811 (2019).
- [47] L. Kong, L. Cao, S. Zhu, M. Papaj, G. Dai, G. Li, P. Fan, W. Liu, F. Yang, X. Wang, S. Du, C. Jin, L. Fu, H. J. Gao, and H. Ding, Majorana zero modes in impurity-assisted vortex of LiFeAs superconductor, *Nat. Commun.* **12**, 1 (2021).
- [48] C.-K. Chiu, T. Machida, Y. Huang, T. Hanaguri, and F.-C. Zhang, Scalable majorana vortex modes in iron-based superconductors, *Sci. Adv.* **6**, eaay0443 (2020).
- [49] K. Jiang, X. Dai, and Z. Wang, Quantum Anomalous Vortex and Majorana Zero Mode in Iron-Based Superconductor Fe(Te,Se), *Phys. Rev. X* **9**, 011033 (2019).
- [50] V. Pathak, S. Plugge, and M. Franz, Majorana bound states in vortex lattices on iron-based superconductors, *Ann. Phys.* **435**, 168431 (2021).
- [51] E. Mascot, S. Cocklin, M. Graham, M. Mashkooi, S. Rachel, and D. K. Morr, Topological surface superconductivity in FeSe_{0.45}Te_{0.55}, *Commun. Phys.* **5**, 188 (2022).
- [52] J. M. Kosterlitz, The critical properties of the two-dimensional xy model, *J. Phys. C* **7**, 1046 (1974).